catalysts

MDPI

Article

Effects of Preparation Method on the Structure and Catalytic Activity of Ag–Fe_2O_3 Catalysts Derived from MOFs

Xiaodong Zhang [1,*], Yang Yang [1], Xutian Lv [1], Yuxin Wang [2] and Lifeng Cui [1,*]

1 School of Environment and Architecture, University of Shanghai for Science and Technology, Shanghai 200093, China; 18602194245@163.com (Y.Y.); 17681925822@163.com (X.L.)

2 Institute of Applied Biotechnology, Taizhou Vocation & Technical College, Taizhou 318000, China; wangyuxin0914@163.com

* Correspondence: fatzhxd@126.com or zhangxiaodong@usst.edu.cn (X.Z.); lifeng.cui@gmail.com (L.C.); Tel.: +86-159-2126-7160 (X.Z.)

Received: 30 October 2017; Accepted: 5 December 2017; Published: 9 December 2017

Abstract: In this work, Ag–Fe_2O_3 catalysts were successfully prepared using several different methods. Our main intention was to investigate the effect of the preparation methods on the catalysts' structure and their catalytic performance for CO oxidation. The catalysts were characterized by X-ray diffraction (XRD), N_2 adsorption–desorption, transmission electron microscopy (TEM), X-ray photoelectron spectroscopy (XPS), H_2-temperature program reduction (H_2-TPR) and inductively coupled plasma optical emission spectroscopy (ICP-OES). Ag–Fe catalysts prepared by impregnating Ag into MIL-100 (Fe) presented the best catalytic activity, over which CO could be completely oxidized at 160 °C. Based on the characterization, it was found that more metallic Ag species and porosity existed on Ag–Fe catalysts, which could efficiently absorb atmospheric oxygen and, thus, enhance the CO oxidation.

Keywords: CO oxidation; MIL-100 (Fe); Ag–Fe_2O_3; preparation method

1. Introduction

Carbon monoxide catalytic oxidation is a typical model for catalyst studies due to its relatively simple surface bimolecular reaction. It has also been used in many industrial reactions, such as low-temperature water–gas shift reaction and fuel cell reaction [1,2]. There are mainly two types of catalysts for CO oxidation, including metal oxides and noble metal catalysts.

In the past few decades, many researchers have paid much attention to developing metal oxide catalysts because of their low economic costs [3–18]. Among the inexpensive transition metal oxides, hematite (α–Fe_2O_3) is an extremely fascinating candidate for potential application values, due to its high resistance to corrosion, abundant resources, low cost, and environmentally friendly properties [19,20]. Therefore, many researchers have focused on Fe_2O_3 nanocatalysts with various structures for CO oxidation [21–23].

Metal–organic frameworks (MOFs) are a kind of porous network material composed of metal atoms and organic ligands, which have high surface areas, tuneable porosity, and a well-defined structure [24–26]. MOFs have attracted much attention as precursors for nanoporous metal oxides [27–30]. Abney et al. [31] levered the advantageous properties of a sacrificial MOF template to form a series of CuO–CeO_2 catalyst systems displaying enhanced CO oxidation performance. Raja et al. [32] also prepared metal and metal oxide nanoparticles, such as Cu–CuO, Co–Co_3O_4, ZnO, Mn_2O_3, MgO, and CdS–CdO, by thermolysis of MOFs. In our previous study, α–Fe_2O_3 catalysts derived from MIL-100 (Fe) achieved a complete conversion for CO being oxidized to CO_2 at 255 °C [30], and its activity can be further improved.

The noble metal catalysts containing Ag [33–35], Au [36,37], Pd [38], In [39] or Pt [40,41] have been used in the catalytic oxidation of CO to CO_2 in the past few decades. Ag is a relatively inexpensive catalyst compared to Pt and Au, showing excellent low-temperature activities for many catalytic reactions, such as NOx abatement [42], ethylene epoxidation [43,44], and methane oxidation [45]. It is generally accepted that supporting Ag on transition metal oxide is beneficial to catalytic performance. Therefore, the exploration focusing on various oxides-supported Ag catalysts has attracted increasing interest.

It is well established that the preparation method has a significant influence on the structural properties and performance of the catalyst. The modifications of the surface area, particle size, dispersion of the active component, and strength of the interaction between the active phase and the support determine the redox properties and the reactivity of the final catalysts [32,46–48]. To the best of our knowledge, very little attention has been focused on comparing the effect of preparation methods for Ag–Fe_2O_3 catalysts derived from MOFs. In this work, we synthesized Ag–Fe_2O_3 catalysts by several different methods. Simultaneously, the Ag–Fe_2O_3 catalytic performances for CO oxidation were evaluated. The mutual relationship between the activity of catalysts and their physicochemical properties will also be discussed in detail.

2. Results and Discussion

2.1. Characterization of Catalysts

XRD patterns of pure α–Fe_2O_3 and Ag–Fe_2O_3 catalysts prepared by various methods are shown in Figure 1 (α–Fe_2O_3 was obtained by calcination of MIL-100 (Fe) at 430 °C for 2 h) [30]. It was found that all samples present two major diffraction lines at 2θ = 33.1° and 35.6°, which correspond to (104) and (110) lattice planes of α–Fe_2O_3 [3] (PDF No. 330664), In the case of the Ag–Fe_2O_3 catalysts being prepared by several different ways, the addition of silver did not change the crystalline structure. In addition, the XRD patterns of a series of Ag–Fe_2O_3 catalysts show diffraction lines at 38.2°, 44.2°, 64.4°, 77.1°, corresponding to the (111), (200), (220), and (311) lattice planes of the cubic structure of Ag, respectively [49], indicating that metal silver particles formed over the supports.

However, weak diffraction lines of silver were detected on the Ag–PB sample, which is probably due to the small particle size of Ag. To investigate the influence of the preparation process on the variation of crystallite size, the mean crystallite sizes of Fe_2O_3 and Ag for all samples were calculated using the Scherrer Formula based on the XRD results and listed in Table 1. It is well known that the smallest average crystallite size of Fe_2O_3 is observed for Ag–Fe (21 nm), while it is ca. 26–27 nm in all other methods. The mean silver grain sizes of Ag–Fe, Ag–MIL, Ag–Fe_2O_3, and Ag–PB samples, calculated from the Ag (111) half-peak broadening (FWHM), were 10, 9, 12, and 8 nm, respectively.

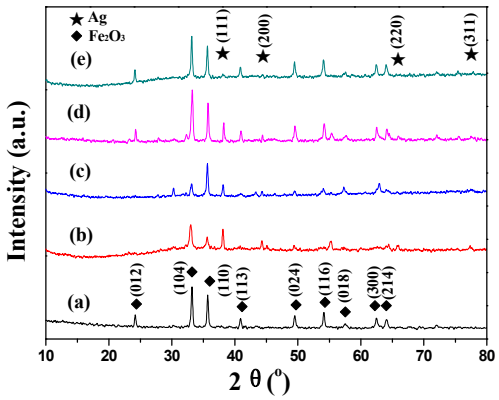

Figure 1. XRD patterns of Fe_2O_3 [30] and Ag catalysts with different preparation methods: (**a**) Fe_2O_3 [30]; (**b**) Ag–Fe; (**c**) Ag–MIL; (**d**) Ag–Fe_2O_3; (**e**) Ag–PB.

Table 1. Textural properties, crystallite size, and composition of the samples.

Catalysts	Textural Properties			Crystallite Size (nm)			Chemical Composition					
	S_{BET} (m^2 g^{-1}) [a]	V (cc g^{-1}) [b]	D (nm) [c]	XRD (nm) [d]			TEM (nm) [e]			ICP-OES (%) [f]		XPS(%) [g]
				Fe	Ag	Ag	Fe	Ag	Ag–Fe_2O_3	Fe	Ag	Ag–Fe
Fe_2O_3 [30]	27	0.21	2.2	26	-	-	69.1	0	0	-	-	-
Ag–Fe	68	0.26	1.5–4, 12–25	21	10	4.7 ± 1.2	65.5	3.41	3.64	6.81	1.78	0.26
Ag–MIL	17	0.06	1.4	26	9	4.5 ± 1.4	62.2	8.26	9.29	6.07	1.72	0.28
Ag–Fe_2O_3	21	0.06	1.7	26	12	5.3 ± 1.0	60.6	5.03	5.81	7.27	1.35	0.19
Ag–PB	21	0.19	1.9	27	8	3.8 ± 0.6	53.2	5.09	6.70	7.76	2.38	0.31

[a] Brunauer–Emmett–Teller (BET) specific surface area; [b] Total pore volume measured at P/P_0 = 0.99; [c] The pore diameter calculated from the desorption branch of the isotherm using the Barrett–Joyner–Halenda (BJH) method; [d] Calculated by Scherrer formulation from the FWHM of Fe_2O_3 (104) and Ag (111) diffraction peak; [e] Measured by transmission electron microscopy (TEM); [f] Element ratio determined by inductively coupled plasma optical emission spectroscopy (ICP-OES); [g] Surface atomic ratio calculated from the X-ray photoelectron spectroscopy (XPS) results.

Figure 2 shows the N_2 adsorption–desorption isotherms (Figure 2A) and the pore size distribution curves (Figure 2B) of Ag catalysts. The isotherms of Fe_2O_3, Ag–Fe, and Ag–PB show the type IV isotherms with an unclosed hysteresis loop at $P/P_0 > 0.8$, indicating that there are interparticle pores or that some impure phases exist. The isotherms of Ag–MIL and Ag–Fe_2O_3 can be classified as type I according to the IUPAC classification. The structural parameters of the catalysts, including BET surface areas, total pore volumes, and the pore diameters are summarized in Table 1.

As a first observation, compared with the pure Fe_2O_3 catalyst, the pore size of Ag–Fe lies mainly in the range of 1.5–4 nm and 12–25 nm, indicating that the catalyst produced by this method can produce many large pores, which results in an increase of BET surface areas from 27 to 68 m^2 g^{-1}. The relatively high surface area might be attributed to the decomposition of nitrates ($AgNO_3$) and organic ligands (MIL-100 (Fe)) simultaneously during preprocessing; a lot of pores are formed in the formation of gases. However, for Ag–MIL, Ag–Fe_2O_3, and Ag–PB, the surface areas and pore diameters decreased with the additional Ag component, which is consistent with most literature reports [50,51].

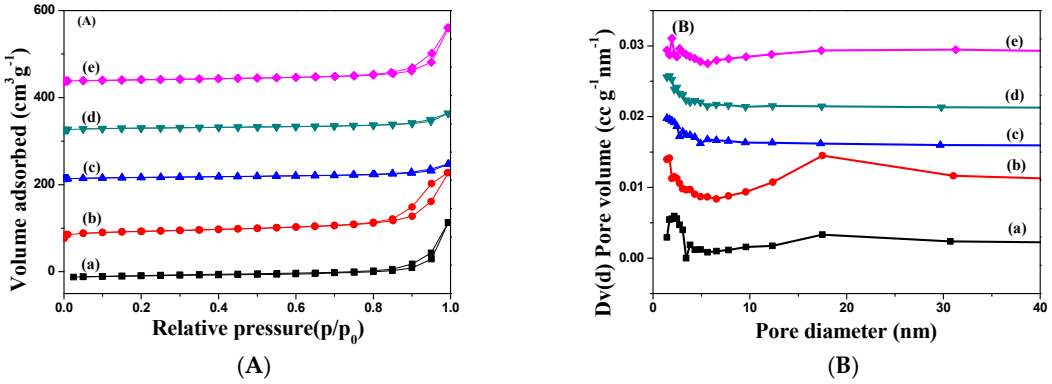

Figure 2. N_2 adsorption–desorption isotherms (**A**) of (**a**) Fe_2O_3 [30]; (**b**) Ag–Fe; (**c**) Ag–MIL; (**d**) Ag–Fe_2O_3; (**e**) Ag–PB and pore size distributions (**B**) of (**a**) Fe_2O_3 [30], (**b**) Ag–Fe, (**c**) Ag–MIL, (**d**) Ag–Fe_2O_3, (**e**) Ag–PB.

The dispersion of noble metal can be significantly affected by the preparation process, implying the diversity in the size distribution of the noble metal particles, which can be confirmed by the TEM images (Figure 3). In the TEM images, highly dispersed silver nanoparticles can be observed on the surface of Ag–MIL and Ag–Fe catalysts. The Ag particle size distributions established, based on the TEM images, are also presented in Figure 3. It can be seen that the mean Ag mean particle size in Ag–Fe is about 4.7 ± 1.2 nm (Figure 3a'), and the average sizes of Ag nanoparticles on Ag–MIL,

Ag–Fe_2O_3 and Ag–PB are about 4.5 ± 1.4 nm (Figure 3b'), 5.3 ± 1 nm (Figure 3c') and 3.8 ± 0.6 nm (Figure 3d'), respectively. The size and distribution of silver nanoparticles were further provided by TEM images, rending it possible to observe the particles with sizes lower than the results obtained using the Scherrer method.

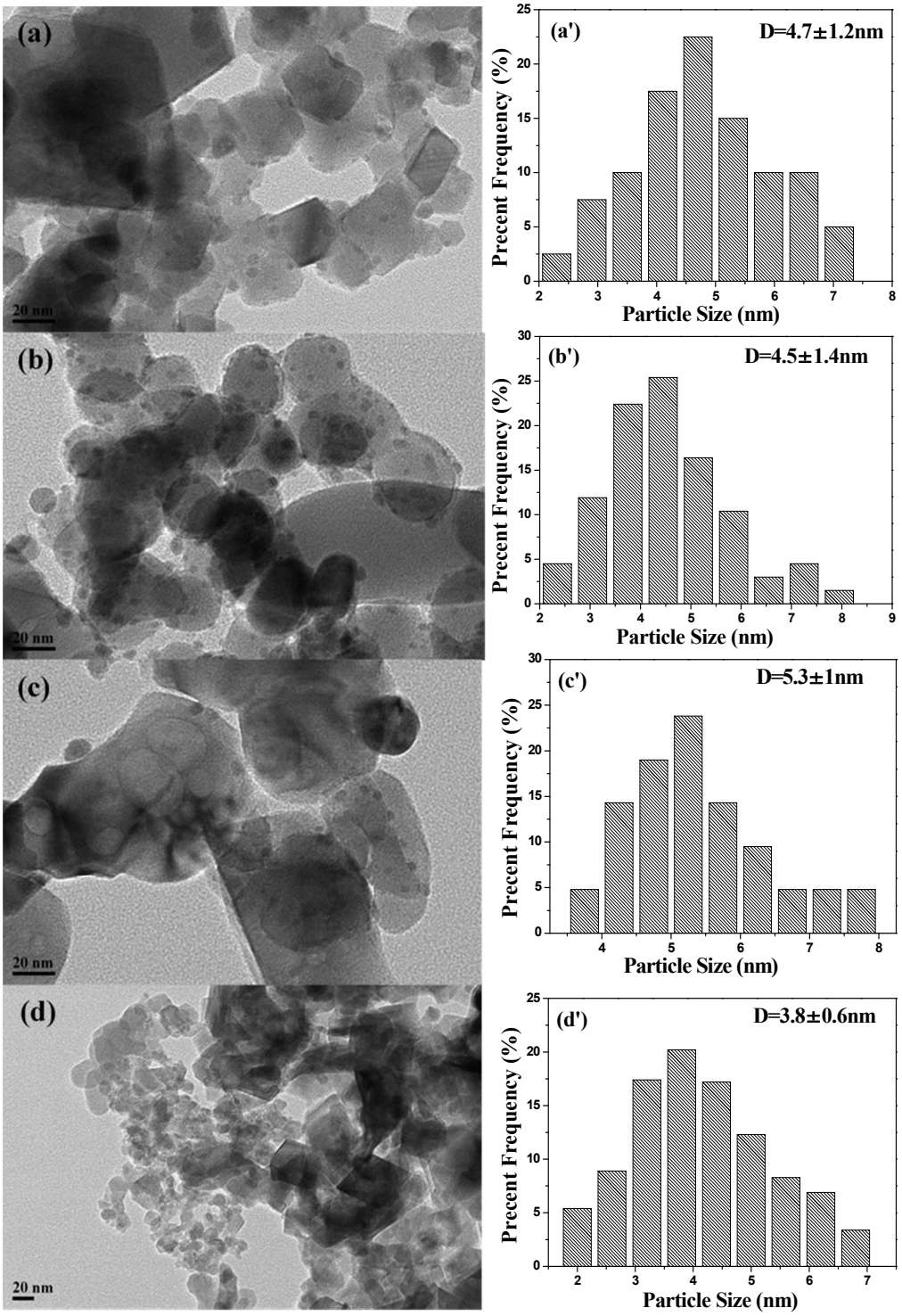

Figure 3. TEM images and particle size distribution of Ag catalysts with different preparation methods (**a**) Ag–Fe; (**b**) Ag–MIL; (**c**) Ag–Fe_2O_3; (**d**) Ag–PB.

The results of TEM and XRD show that the sizes and size distribution of Ag particles could be affected by the preparation method. In addition, it can be seen from Figure 3 that the morphologies of the Fe_2O_3 supporters are slightly different shapes due to the different preparation methods. The Ag–Fe catalyst maintains the brick-like shape of MIL-100 (Fe), Ag–MIL and Ag–Fe_2O_3 present the irregular appearance of different sizes, and Ag–PB shows a smaller block or polyhedron morphology.

The results of inductively coupled plasma optical emission spectroscopy (ICP-OES) analysis for the samples synthesized by different methods are listed in Table 1. It can be found that the chemical compositions of materials are not very close to the theoretically expected ones, except for Ag–MIL. The results showed that the Ag–Fe_2O_3 actual weight loading determined for Ag–Fe, Ag–MIL, Ag–Fe_2O_3, and Ag–PB materials are of 3.64%, 9.29%, 5.81%, and 6.70%, respectively. These results show that the in-situ synthesis can minimize the loss of silver, and three other methods of introducing silver can result in a big loss, especially for Ag–Fe catalyst. Moreover, bulk Ag to Fe_2O_3 ratios (from ICP-OES) seem to be higher than surface Ag to Fe ratios (determined from XPS), which indicates the inclusion of the Ag particle into the Fe_2O_3 matrix.

In order to investigate the redox properties of the Ag catalyst prepared by different methods, H_2-temperature program reduction (H_2-TPR) measurements were carried out, as shown in Figure 4. There are two main H_2-consumption peaks in the experimental temperature range for all catalysts; the peak at lower temperatures is attributed to the reduction process of Fe_2O_3 to Fe_3O_4 and the other broad peak at higher temperatures is associated with the transformations of $Fe_3O_4 \rightarrow FeO \rightarrow Fe^0$ [33]. It is worth noting that the temperature of reduction peaks of Fe_2O_3 to Fe_3O_4 over the Ag–Fe catalyst (at 170 °C) is much lower than the other three catalysts, indicating that Fe_2O_3 can be more easily reduced by introducing Ag impregnated in MIL-100 (Fe). Meanwhile, the temperature of reduction peaks of Fe_2O_3 to Fe_3O_4 over Ag–MIL, Ag–Fe_2O_3, and Ag–PB are 384 °C, 362 °C, and 502 °C, respectively. Among all the Ag catalysts, Ag–Fe shows the lowest temperature, indicating that its reducibility is stronger. Thus, this catalyst seems to be beneficial to the CO oxidation reaction.

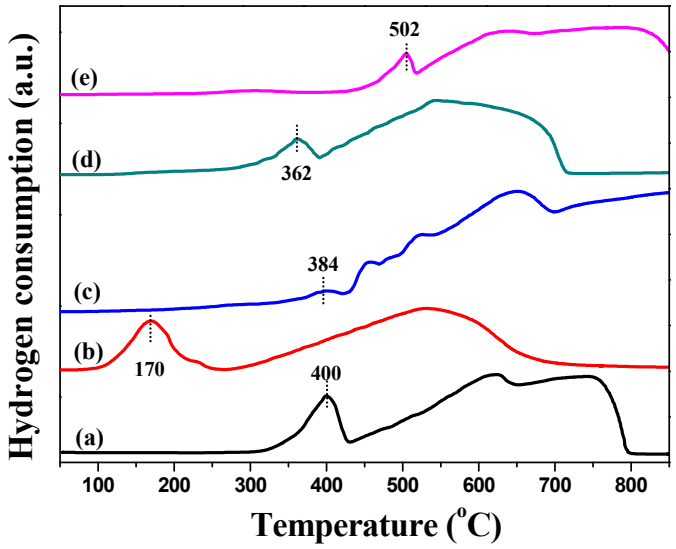

Figure 4. H_2-temperature program reduction (H_2-TPR) results of (**a**) Fe_2O_3 [30]; (**b**) Ag–Fe; (**c**) Ag–MIL; (**d**) Ag–Fe_2O_3; (**e**) Ag–PB.

The XPS characterizations were carried out to further investigate the relationships between surface chemical species and catalytic performance on the catalyst. As shown in Figure 5 and Table 2, The high-resolution Ag-3d XPS spectrum shows two individual broad peaks located at about 368.1 eV and 374.4 eV (Figure 5A), which are assigned to metallic Ag $3d_{5/2}$ and Ag $3d_{3/2}$ levels, respectively. The $3d_{5/2}$ peak can be resolved into two peaks located at about 368.2 eV and 367.6 eV, which can be attributed to metallic Ag^0 and silver oxide species, respectively [51,52]. A quantitative analysis

of surface $Ag^0/Ag^{\delta+}$ molar ratios on the Ag $3d_{5/2}$ XPS spectra of Ag–Fe_2O_3 catalysts with different preparation methods is summarized in Table 2. As the preparation method changes, $Ag^0/Ag^{\delta+}$ molar ratios of Ag–Fe, Ag–MIL, Ag–Fe_2O_3, and Ag–PB are 2.00, 0.97, 1.17, and 1.37, respectively.

As shown in Figure 5B, the Fe-2p spectrum is comprised of two characteristic binding energy peaks at 710.9 eV for $Fe2p_{3/2}$ and 724.6 eV for $Fe2p_{1/2}$. The peak separation between Fe $2p_{3/2}$ and Fe $2p_{1/2}$ peaks is about 13.7 eV, indicating the formation of the α–Fe_2O_3. The peaks at 710.9 eV can be fitted with two peaks of 712.8 and 710.7 eV, which are attributed to Fe (II) and Fe (III) species [53]. Fe^{2+}/Fe^{3+} molar ratios also change with the preparation methods changes. As Table 2 shows, the Fe^{2+}/Fe^{3+} molar ratios of Ag–Fe, Ag–MIL, Ag–Fe_2O_3, and Ag–PB are 1.38, 0.71, 0.51, and 0.68, respectively.

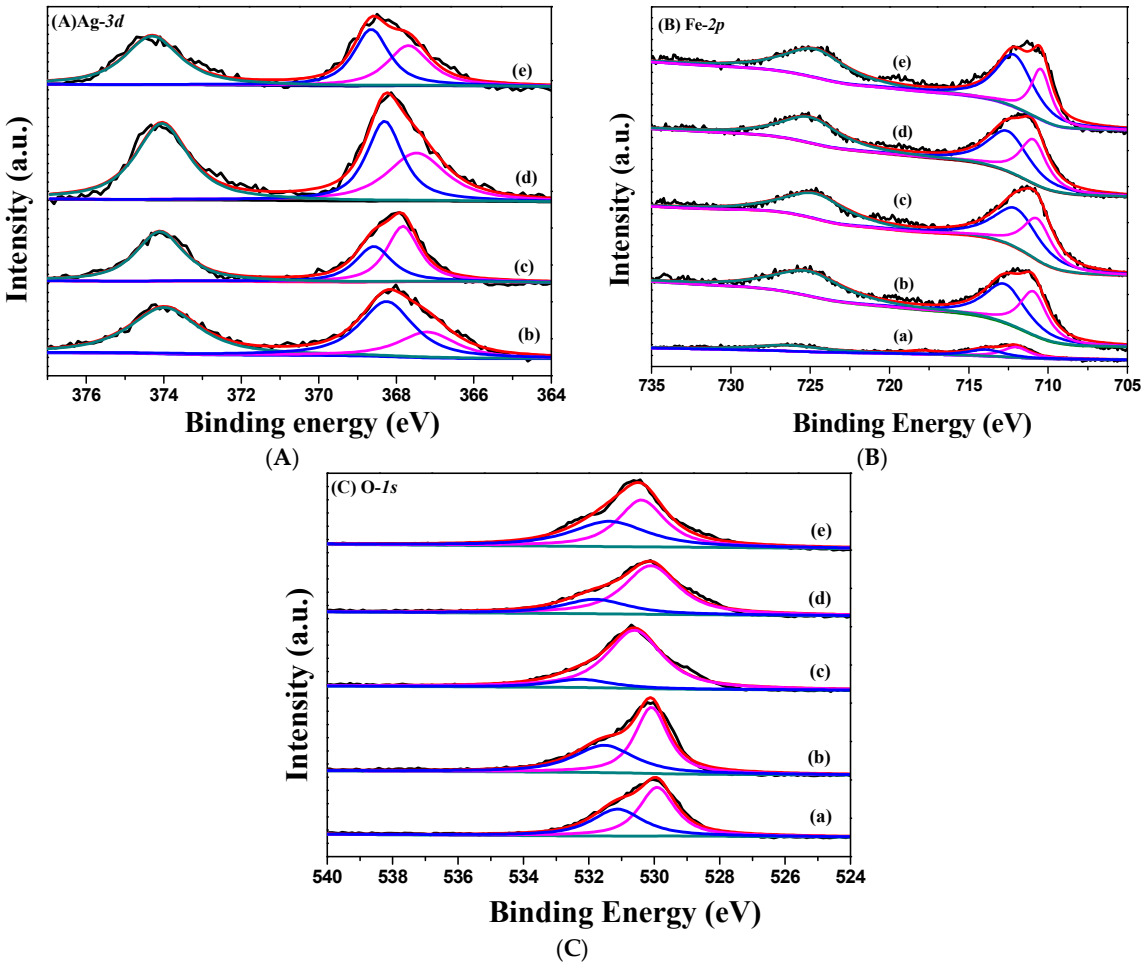

Figure 5. XPS spectra of Ag-3d (**A**), Fe-2p; (**B**) and O-1s; (**C**), (**a**) Fe_2O_3, (**b**) Ag–Fe, (**c**) Ag–MIL, (**d**) Ag–Fe_2O_3, (**e**) Ag–PB.

Table 2. XPS species molar ratio of the synthesized Ag–Fe_2O_3 catalysts with different preparation methods.

Catalysts	$Ag^0/Ag^{\delta+}$	Fe^{2+}/Fe^{3+}	O_{latt}/O_{ads}
Fe_2O_3	-	1.24	1.27
Ag–Fe	2.00	1.38	2.78
Ag–MIL	0.97	0.71	6.05
Ag–Fe_2O_3	1.17	0.51	1.32
Ag–PB	1.37	0.68	1.15

Figure 5C shows the XPS spectrum of O-1s, fitted by two bending energy peaks of about 530.1 eV and 532.1 eV. The peaks at 530.1 eV can be attributed to oxygen species corresponding to Fe_2O_3,

while the other peak at 532.1 eV can be related to oxygen in the electrophilic state adsorbed on Ag [54]. As Table 2 shows, the O_{latt}/O_{ads} molar ratios of Ag–Fe, Ag–MIL, Ag–Fe_2O_3 and Ag–PB are 2.78, 6.05, 1.32, and 1.15, respectively.

2.2. Catalytic Performance

The catalytic behaviors of the Ag–Fe_2O_3 catalysts with various preparation methods toward CO oxidation are shown in Figure 6. All samples were calcined for 2 h at 430 °C in muffle furnaces before testing. It was found that the preparation method markedly influenced the catalytic activity. It is obvious that the Ag–Fe catalyst shows outstanding catalytic activity for the CO oxidation (T_{100} = 160 °C). However, the total conversion temperatures of Ag–MIL, Ag–Fe_2O_3, and Ag–PB toward CO oxidation are 275 °C, 220 °C, and 480 °C, respectively. In order to get more detailed comparison about the activity of CO oxidation for different silver catalysts, several catalysts have been listed in Table 3. The Ag–Fe catalysts prepared in this work show higher activity for complete conversion than those reported ones [50–56].

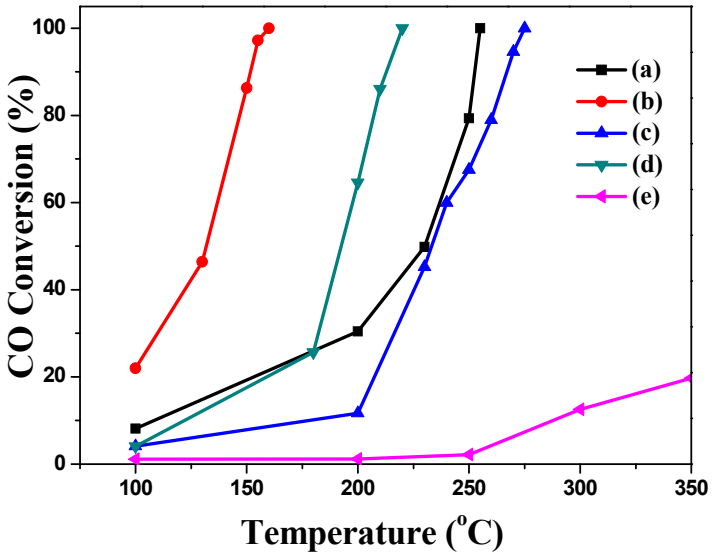

Figure 6. CO conversion over Fe_2O_3 and Ag catalysts with different preparation methods (**a**) Fe_2O_3 [30]; (**b**) Ag–Fe; (**c**) Ag–MIL; (**d**) Ag–Fe_2O_3; (**e**) Ag–PB.

Table 3. Comparison of the activity for CO oxidation on different catalysts.

Catalysts	Ag Loading (wt %)	Flow Rate (mL min^{-1})	T_{10} (°C)	T_{50} (°C)	T_{98} (°C)	References
Fe_2O_3	0	30	110	230	253	[30]
Ag–Fe	3.64	30	<100	132	157	This work
Ag–MIL	9.29	30	190	230	275	This work
Ag–Fe_2O_3	5.81	30	120	≈180	215	This work
Ag–PB	6.70	30	290	>350	>350	This work
Ag–Fe_2O_3	≈20	100	≈110	≈150	≈270	[50]
Ag–Fe_2O_3	6.7	30	<50	80	≈200	[51]
Ag–Co_3O_4	-	30	≈50	≈85	100	[52]
Pd/α–Fe_2O_3	1.04	200	-	-	20	[55]
Au/α–Fe_2O_3	0.74	200	≈50	>75	>75	[56]

It is worth noting that the preparation methods show a great influence on the structure and activity of the catalysts, according to the results of the catalyst characterization and the activity test results. The smaller size of crystalline Fe_2O_3 (XRD), as well as its relatively high surface area, are

observed in Ag–Fe catalyst. It can also be found that Ag–Fe prepared in this way has a highly dispersed, uniform silver particle on its surface (TEM). According to the H_2-TPR results, Ag–Fe is more likely to be reduced at lower temperatures. Moreover, the Ag–Fe catalyst shows the optimal $Ag^0/Ag^{\delta+}$ ratios. The addition of Ag changes the distribution of original Fe^{2+}/Fe^{3+}, showing that a larger ratio of Fe^{2+}/Fe^{3+} is favorable to form more oxygen vacancies [57] and is also much more abundant in surface lattice oxygen species, which are favorable to the adsorption and activation of CO molecules [57].

In addition, the Ag–Fe catalyst absorbs more atmospheric oxygen, which most likely represents the oxygen supply during the oxidation reaction. The increase in activity has often been ascribed to the oxygen donation from the surface transition metal oxide sites to the silver species [58]. When the catalyst was prepared by impregnating Ag into MIL-100 (Fe) and pretreated in a muffle furnace at 430 °C (Ag–Fe), the carrier MIL-100 (Fe) is decomposed into small size Fe_2O_3 with the formation of large pores and larger specific surface areas, which is likely due to the decomposition of nitrate. In the meantime, the organic ligands of MIL-100 (Fe) were decomposed to produce reducing gases, which promote the formation of Ag^0.

3. Materials and Methods

3.1. Catalyst Preparation

MIL-100 (Fe) was prepared by a traditional hydrothermal method [59] according to a given amount of iron powder (0.654 g), 1, 3, 5-benzenetricarboxylic acid (1, 3, 5-BTC,1.76 g), a given volume of hydrofluoric acid (1.02 mL), nitric acid (0.48 mL) and pure water (56.9 mL), where the component ratio of n (Fe):n (1,3,5-BTC):n (HF):n (HNO_3):n (H_2O) = 1:0.67:2:0.6:277. After continuous stirring for five minutes, the mixture was transferred to a polypropylene bottle and subsequently placed into an oven at 150 °C for 12 h. After cooling to room temperature naturally, the resulting solid was collected by filtration, washed with deionized water and dried under 80 °C for 12 h to get light orange bulk crystals. The dried samples were further purified with ethanol under the condition of 70 °C for 4 h, then washed with deionized water and dried under 80 °C for 12 h to obtain high purity MIL-100 (Fe).

Scheme 1 illustrates the specific process for generating the Ag–Fe_2O_3 composite catalysts (Fe/Ag ratio of 15) used in this study: (i) Silver catalysts supported on MIL-100 (Fe) support were synthesized by a conventional incipient wetness impregnation method [2]. A given amount of $AgNO_3$ precursor solution was dropped slowly to MIL-100 (Fe) support with constant stirring, then the sample was aged at room temperature overnight and dried at 70 °C for 12 h. The final product was named as Ag–Fe.

In addition, we also used three methods to prepare the Ag–Fe_2O_3 catalysts. (ii) The synthesis process is the same as the synthesis of MIL-100 (Fe), except that a given amount of silver is added during the agitation process before hydrothermal treatment; the final product was named as Ag-MIL. (iii) The Fe_2O_3 was used as the carrier, which derived from MIL-100 (Fe) with calcination for 2 h at 430 °C in a muffle furnace [30], and the silver was impregnated into the Fe_2O_3 as before, while the final catalyst was denoted as Ag–Fe_2O_3. iv) Commercial Prussian blue ($C_{18}Fe_7N_{18}$) was used as the support, and the silver was loaded by the impregnation method as before which was denoted as Ag–PB. All as-prepared samples were calcined at 430 °C for 2 h in a muffle furnace and kept in a drying vessel. Before any characterization and tests, the samples were purged at 100 °C for 30 min with Ar atmosphere.

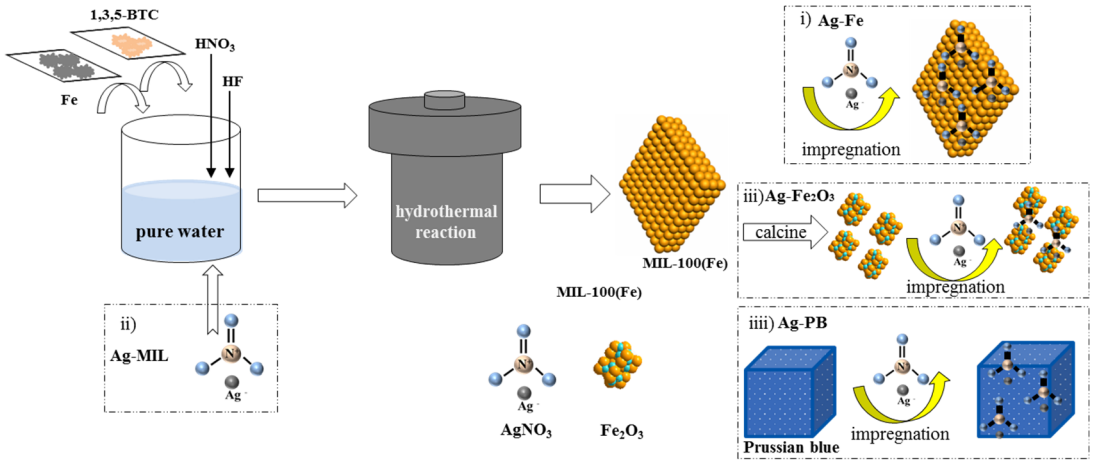

Scheme 1. Synthetic route of Ag–Fe_2O_3 catalysts with different preparation methods.

3.2. Catalysts Characterization

X-ray powder diffraction (XRD) characterizations were performed with a Bruker D8 Advance instrument, employing a Copper Kα radiation monochromatic detector, which with λ = 1.5418 Å at an accelerating voltage of 40 kV and an emission current 40 mA, the sample was scanned in the range between 10° and 80° with a scan rate of 5°·min^{-1}. N_2 adsorption–desorption isotherms were obtained on a Quantachrome autosorb-iQ-2MP. The Brunauer–Emmett–Teller (BET) method was used to calculate the specific surface areas; pore size distribution curves were determined from the adsorption branches calculated by the Barrett–Joyner–Halenda (BJH) method. Transmission electron microscopy (TEM) images were obtained by using a JEM 2100 instrument, and the acceleration voltage was 200 kV. Temperature programmed reduction (TPR) experiments were carried out with a ChemBET TPR/TPD instrument, where the flow was fed with 10 vol.% H_2 and balanced with Ar. 0.05 g samples, which were reduced in a flow of H_2–Ar mixture. The temperature increased from room temperature to 850 °C with a heating rate of 10 °C·min^{-1}. X-ray photoelectron spectroscopy (XPS) relevant data were recorded by ThermoFisher with Al Kα source, and the binding energies were calibrated internally by the carbon deposit C-1s binding energy (BE) at 284.6 eV. Metal content was carried out by an inductively coupled plasma optical emission spectroscopy (ICP-OES), which was performed on Optima 8000 PE.

3.3. Catalytic Activity Measurements

The performance of catalysts for CO oxidation was evaluated in a continuous flow fixed-bed reactor system; the outer diameter of quartz microreactor is 6 mm. The 0.1 g catalysts (20–40 mesh) were used for CO oxidation testing at the atmospheric pressure. The reactants were fed with a volume ratio of $He/CO/O_2$ = 79/1/20 (a total flow rate of 30 mL min^{-1}) controlled by independent thermal mass flow controllers. The concentrations of CO were analyzed after the reaction process became stable by using on-line gas chromatograph (GC 2060) with a thermal conductivity detector (TCD). In this paper, the CO conversion was calculated from the CO concentration of inlet and outlet gases:

$$\text{CO conversion} = ([\text{CO}]\text{in} - [\text{CO}]\text{out})/[\text{CO}]\text{in} \times 100\%$$

where [CO]in is the inlet CO concentration and [CO]out is the outlet CO concentration. In previous experiments, we measured the conversion rates by detecting CO_2, and the results are consistent with the CO calculation, and there was no hydrogen produced during the catalytic process by mass spectrometry.

4. Conclusions

According to the structural characterizations and catalytic activity evaluation results, it can be found that the preparation method has a great influence on the structure of catalysts and catalytic performance. It can be reasonably assumed that Ag^0 species and porosity are the main factors for excellent catalytic performance, which was established via impregnating Ag into MIL-100 (Fe) and calcination for 2 h at 430 °C in a muffle furnace. It is worth noting that the simultaneous decomposition of organic ligands and nitrates is beneficial to the formation of Ag^0 species and larger specific surface areas. All these advantages are attributed to the Ag–Fe catalyst prepared by impregnating Ag to MIL-100 (Fe), a route which could be employed as a general method for preparing other noble-metal supported catalysts.

Acknowledgments: This work was sponsored financially by the National Natural Science Foundation of China (No. 21507086, 51508327, 41673093) and Shanghai Sailing Program (14YF1409900, 16YF1408100). Thanks to Anhui Kemi Machinery Technology Co., Ltd. for providing the Teflon-lined stainless steel autoclave.

Author Contributions: Xiaodong Zhang conceived and designed the experiments; Yang Yang performed the experiments and analyzed the data; Xutian Lv, Yuxin Wang, and Lifeng Cui provided the concept of this research and managed all of the experimental and writing processes as the corresponding authors.

Conflicts of Interest: The authors declare no conflict of interest.

References

1. Gardner, S.D.; Upchurch, B.T.; Schryer, D.R.; Kielin, E.J.; Schryer, J. Comparison of the performance characteristics of Pt-SnO_x and Au-MnO_x catalysts for low-temperature CO oxidation. *J. Catal.* **1991**, *129*, 114–120. [CrossRef]
2. Zhang, X.D.; Qu, Z.P.; Li, X.Y.; Wen, M.; Quan, X.; Ma, D.; Wu, J.J. Studies of silver species for low-temperature CO oxidation on Ag/SiO_2 catalysts. *Sep. Purif. Technol.* **2010**, *72*, 395–400. [CrossRef]
3. Pan, H.; Jian, Y.F.; Chen, C.W.; He, C.; Hao, Z.P.; Liu, H.X.; Shen, Z.X. Nanosphere-shaped Mn_3O_4 catalyst with remarkable for low-temperature activity for methyl-ethyl-ketone catalytic combustion of Methyl-ethyl-ketone. *Environ. Sci. Technol.* **2017**, *51*, 6288–6297. [CrossRef] [PubMed]
4. Shen, Q.; Zhang, L.Y.; Sun, N.N.; Wang, H.; Zhong, L.S.; He, C.; Wei, W.; Sun, Y.H. Hollow MnOx/CeO_2 mixed oxides as highly efficient catalysts in NO oxidation. *Chem. Eng. J.* **2017**, *322*, 46–55. [CrossRef]
5. Yu, Y.K.; Miao, J.F.; Wang, J.X.; He, C.; Chen, J.S. Facile synthesis of $CuSO_4$/TiO_2 catalysts with broad temperature window, superior activity and SO_2 tolerance for NH_3-SCR: Physicochemical property and reaction mechanism. *Catal. Sci. Technol.* **2017**, *7*, 1590–1601. [CrossRef]
6. Zhang, X.D.; Li, H.X.; Yang, Y.; Zhang, T.T.; Wen, X.; Liu, N.; Wang, D.J. Facile synthesis of new efficient Cu/MnO_2 catalysts from used battery for CO oxidation. *J. Environ. Chem. Eng.* **2017**, *5*, 5179–5186. [CrossRef]
7. Yang, Y.Q.; Dong, H.; Wang, Y.; Wang, Y.X.; Liu, N.; Wang, D.J.; Zhang, X.D. A facile synthesis for porous CuO/Cu_2O composites derived from MOFs and their superior catalytic performance for CO oxidation. *Inorg. Chem. Commun.* **2017**, *86*, 74–77. [CrossRef]
8. Weng, X.L.; Zeng, Q.S.; Zhang, Y.L.; Dong, F.; Wu, Z.B. Facile Approach for the Syntheses of Ultrafine TiO_2 Nanocrystallites with Defects and C Heterojunction for Photocatalytic Water Splitting. *ACS Sustain. Chem. Eng.* **2016**, *4*, 4314–4320. [CrossRef]
9. Sun, P.F.; Wang, W.L.; Dai, X.X.; Weng, X.L.; Wu, Z.B. Mechanism study on catalytic oxidation of chlorobenzene over $Mn_xCe_{1-x}O_2$/H-ZSM5 catalysts under dry and humid conditions. *Appl. Catal. B Environ.* **2016**, *198*, 389–397. [CrossRef]
10. Yang, X.Q.; Yu, X.L.; Lin, M.Y.; Ge, M.F.; Zhao, Y.; Wang, F.Y. Interface effect of mixed phase Pt/ZrO_2 catalysts for HCHO oxidation at ambient temperature. *J. Mater. Chem. A* **2017**, *5*, 13799–13806. [CrossRef]
11. Meng, Q.J.; Wang, W.J.; Weng, X.L.; Liu, Y.; Wang, H.Q.; Wu, Z.B. Active oxygen species in $La_{n+1}Ni_nO_{3n+1}$ layered perovskites for catalytic oxidation of toluene and methane. *J. Phys. Chem. C* **2016**, *120*, 3259–3266. [CrossRef]
12. Wang, W.L.; Meng, Q.J.; Weng, X.L.; Wu, Z.B. Rapid syntheses of ultrafine $LaMnO_3$ nano-crystallites with superior activity for catalytic oxidation of toluene. *Catal. Commun.* **2016**, *84*, 167–170. [CrossRef]

13. Weng, X.L.; Dai, X.X.; Zeng, Q.S.; Liu, Y.; Wu, Z.B. DRIFT studies on promotion mechanism of $H_3PW_{12}O_{40}$ in selective catalytic reduction of NO with NH_3. *J. Colloid Interface Sci.* **2016**, *461*, 9–14. [CrossRef] [PubMed]
14. Zou, X.J.; Dong, Y.Y.; Zhang, X.D.; Cui, Y.B.; Qu, X.X.; Qi, X.H. The highly enhanced visible light photocatalytic degradation of gaseous o-dichlorobenzene through fabricating like-flowers $BiPO_4$/BiOBr p-n heterojunction composites. *Appl. Surf. Sci.* **2017**, *391*, 525–534. [CrossRef]
15. Wang, Y.X.; Yang, Y.Q.; Xi, L.M.; Zhang, X.D.; Jia, M.H.; Xu, H.M.; Wu, H.G. A simple hydrothermal synthesis of flower-like ZnO microspheres and their improved photocatalytic activity. *Mater. Lett.* **2016**, *180*, 55–58. [CrossRef]
16. Zhang, X.D.; Wang, Y.X.; Hou, F.L.; Li, H.X.; Yang, Y.; Yang, Y.Q.; Wang, Y. Effects of Ag loading on structural and photocatalytic properties of flower-like ZnO microspheres. *Appl. Surf. Sci.* **2017**, *391*, 476–483. [CrossRef]
17. Yang, Y.Q.; Li, H.X.; Hou, F.L.; Hu, J.Y.; Zhang, X.D.; Wang, Y.X. Facile synthesis of ZnO/Ag nanocomposites with enhanced photocatalytic properties under visible light. *Mater. Lett.* **2016**, *180*, 97–100. [CrossRef]
18. Zou, X.J.; Dong, Y.Y.; Zhang, X.D.; Cui, Y.B. Synthesize and characterize of Ag_3VO_4/TiO_2 nanorods photocatalysts and its photocatalytic activity under visible light irradiation. *Appl. Surf. Sci.* **2016**, *366*, 173–180. [CrossRef]
19. Chen, J.; Xu, L.N.; Li, W.Y.; Gou, X.L. α-Fe_2O_3 nanotubes in gas sensor and lithium-ion battery applications. *Adv. Mater.* **2005**, *17*, 582–586. [CrossRef]
20. Wang, Y.; Cao, J.L.; Wang, S.R.; Guo, X.Z.; Zhang, J.; Xia, H.J.; Zhang, S.M.; Wu, S.H. Facile Synthesis of Porous alpha-Fe_2O_3 Nanorods and Their Application in Ethanol Sensors. *J. Phys. Chem. C* **2008**, *112*, 17804–17808. [CrossRef]
21. Wang, L.; Li, Q.; Qin, W.; Zheng, Z.M.; Xiao, X.B.; Dong, C.Q. Activity of Fe_2O_3 and its effect on CO oxidation in the chemical looping combustion: A theoretical account. *Adv. Environ. Technol.* **2013**, *726–731*, 2040–2044.
22. Liu, X.J.; Liu, J.F.; Chang, Z.; Sun, X.M.; Li, Y.D. Crystal plane effect of Fe_2O_3 with various morphologies on CO catalytic oxidation. *Catal. Commun.* **2011**, *12*, 530–534. [CrossRef]
23. Gao, Q.X.; Wang, X.F.; Di, J.L.; Wu, X.C.; Tao, Y.R. Enhanced catalytic activity of α-Fe_2O_3 nanorods enclosed with {110} and {001} planes for methane combustion and CO oxidation. *Catal. Sci. Technol.* **2011**, *1*, 574–577. [CrossRef]
24. Zhang, X.D.; Hou, F.L.; Li, H.X.; Yang, Y.; Wang, Y.X.; Liu, N.; Yang, Y.Q. A strawsheave-like metal organic framework Ce-BTC derivative containing high specific surface area for improving the catalytic activity of CO oxidation reaction. *Microporous Mesoporous Mater.* **2017**. [CrossRef]
25. Liu, N.; Huang, W.Y.; Zhang, X.D.; Tang, L.; Wang, L.; Wang, Y.X.; Wu, M.H. Ultrathin graphene oxide encapsulated in uniform MIL-88A(Fe) for enhanced visible light-driven photodegradation of RhB. *Appl. Catal. B* **2017**, *221*, 119–128. [CrossRef]
26. Zhang, X.D.; Yang, Y.; Huang, W.Y.; Yang, Y.Q.; Wang, Y.X.; He, C.; Liu, N.; Wu, M.H.; Tang, L. g-C_3N_4/UiO-66 nanohybrids with enhanced photocatalytic activities for the oxidation of dye under visible light irradiation. *Mater. Res. Bull.* **2017**. [CrossRef]
27. Zhang, X.D.; Li, H.X.; Hou, F.L.; Yang, Y.; Dong, H.; Liu, N.; Wang, Y.; Cui, L.F. Synthesis of highly efficient Mn_2O_3 catalysts for CO oxidation derived from Mn-MIL-100. *Appl. Surf. Sci.* **2017**, *411*, 27–33. [CrossRef]
28. Zhang, R.R.; Hu, L.; Bao, S.X.; Li, R.; Gao, L.; Li, R.; Chen, Q.W. Surface polarization enhancement: High catalytic performance of Cu/CuOx/C nanocomposites derived from Cu-BTC for CO oxidation. *J. Mater. Chem. A* **2016**, *4*, 8412–8420. [CrossRef]
29. Zhang, X.D.; Hou, F.L.; Yang, Y.; Wang, Y.; Liu, N.; Chen, D.; Yang, Y.Q. A facile synthesis for cauliflower like CeO_2 catalysts from Ce-BTC precursor and their catalytic performance for CO oxidation. *Appl. Surf. Sci.* **2017**, *423*, 771–779. [CrossRef]
30. Cui, L.F.; Zhao, D.; Yang, Y.; Wang, Y.G.; Zhang, X.D. Synthesis of highly efficient α-Fe_2O_3 catalysts for CO oxidation derived from MIL-100(Fe). *J. Solid State Chem.* **2017**, *247*, 168–172. [CrossRef]
31. Abney, C.W.; Patterson, J.T.; Gilhula, J.C.; Wang, L.; Hensley, D.K.; Chen, J.H.; Foo, G.S.; Wu, Z.L.; Dai, S. Controlling Interfacial Properties in Supported Metal Oxide Catalysts through Metal-Organic Framework Templating. *J. Mater. Chem. A* **2017**, *26*, 13565–13572. [CrossRef]
32. Das, R.; Pachfule, P.; Banerjee, R.; Poddar, P. Metal and metal oxide nanoparticle synthesis from metal organic frameworks (MOFs): Finding the border of metal and metal oxides. *Nanoscale* **2012**, *4*, 591–599. [CrossRef] [PubMed]

33. Yang, F.; Huang, J.L.; Odoom-Wubah, T.; Hong, Y.L.; Du, M.M.; Sun, D.H.; Jia, L.S.; Li, Q.B. Efficient Ag/CeO_2 catalysts for CO oxidation prepared with microwave-assisted biosynthesis. *Chem. Eng. J.* **2015**, *269*, 105–112. [CrossRef]
34. Zhang, X.D.; Dong, H.; Zhao, D.; Wang, Y.; Wang, Y.G.; Cui, L.F. Effect of support calcination temperature on Ag structure and catalytic activity for CO oxidation. *Chem. Res. Chin. Univ.* **2016**, *32*, 455–460. [CrossRef]
35. Yang, Y.Q.; Hou, F.L.; Li, H.X.; Liu, N.; Wang, Y.; Zhang, X.D. Facile synthesis of Ag/KIT-6 catalyst via a simple one pot method and application in the CO oxidation. *J. Porous Mater.* **2017**, *24*, 1661–1665. [CrossRef]
36. Somodi, F.; Borbath, I.; Hegedus, M.; Tompos, A.; Sajo, I.E.; Szegedi, A.; Rojas, S.; Garcia Fierro, J.L.; Margitfalvi, J.L. Modified preparation method for highly active Au/SiO_2 catalysts used in CO oxidation. *Appl. Catal. A* **2008**, *347*, 216–222. [CrossRef]
37. Daniells, S.T.; Overweg, A.R.; Makkee, M.; Moulijn, J.A. The mechanism of low-temperature CO oxidation with Au/Fe_2O_3 catalysts: A combined Mossbauer, FT-IR, and TAP reactor study. *J. Catal.* **2005**, *230*, 52–65. [CrossRef]
38. Jiang, X.C.; Yu, A.B. Synthesis of Pd/alpha-Fe_2O_3 nanocomposites for catalytic CO oxidation. *J. Mater. Process. Technol.* **2009**, *209*, 4558–4562. [CrossRef]
39. Pan, H.; Jian, Y.F.; Yu, Y.K.; He, C.; Shen, Z.X.; Liu, H.X. Regeneration and sulfur poisoning of In/H-BEA catalyst for NOx reduction by CH_4. *Appl. Surf. Sci.* **2017**, *401*, 120–126. [CrossRef]
40. Hoseini, S.J.; Bahrami, M.; Roushani, M. High CO tolerance of Pt/Fe/Fe_2O_3 nanohybrid thin film suitable for methanol oxidation in alkaline medium. *RSC Adv.* **2014**, *4*, 46992–46999. [CrossRef]
41. Lin, M.Y.; Yu, X.L.; Yang, X.Q.; Li, K.Z.; Ge, M.F.; Li, J.H. Highly active and stable interface derived from Pt supported on Ni/Fe layered double oxides for HCHO oxidation. *Catal. Sci. Technol.* **2017**, *7*, 1573–1580. [CrossRef]
42. He, H.; Yu, Y.B. Selective catalytic reduction of NOx over Ag/Al_2O_3 catalyst: From reaction mechanism to diesel engine test. *Catal. Today* **2005**, *100*, 37–47. [CrossRef]
43. Christopher, P.; Linic, S. Engineering selectivity in heterogeneous catalysis: Ag nanowires as selective ethylene epoxidation catalysts. *J. Am. Chem. Soc.* **2008**, *130*, 11264–11265. [CrossRef] [PubMed]
44. Piccinin, S.; Zafeiratos, S.; Stampfl, C.; Hansen, T.W.; Haevecker, M.; Teschner, D.V.; Bukhtiyarov, I.; Girgsdies, F.; Knop-Gericke, A.; Schloegl, R.; et al. Alloy Catalyst in a Reactive Environment: The Example of Ag-Cu Particles for Ethylene Epoxidation. *Phys. Rev. Lett.* **2010**, *104*. [CrossRef] [PubMed]
45. Kundakovic, L.; Flytzani-Stephanopoulos, M. Deep oxidation of methane over zirconia supported Ag catalysts. *Appl. Catal. A* **1999**, *183*, 35–51. [CrossRef]
46. Zhang, X.D.; Qu, Z.P.; Jia, J.X.; Wang, Y. Ag nanoparticles supported on wormhole HMS material as catalysts for CO oxidation: Effects of preparation methods. *Powder Technol.* **2012**, *230*, 212–218. [CrossRef]
47. Shiau, C.Y.; Ma, M.W.; Chuang, C.S. CO oxidation over CeO_2-promoted Cu/gamma-Al_2O_3 catalyst: Effect of preparation method. *Appl. Catal. A* **2006**, *301*, 89–95. [CrossRef]
48. Avgouropoulos, G.; Ioannides, T.; Matralis, H. Influence of the preparation method on the performance of CuO-CeO_2 catalysts for the selective oxidation of CO. *Appl. Catal. B* **2005**, *56*, 87–93. [CrossRef]
49. Zhang, X.D.; Qu, Z.P.; Li, X.Y.; Zhao, Q.D.; Wang, Y.; Quan, X. Low temperature CO oxidation over Ag/SBA-15 nanocomposites prepared via in-situ "pH-adjusting" method. *Catal. Commun.* **2011**, *16*, 11–14. [CrossRef]
50. Biabani-Ravandi, A.; Rezaei, M.; Fattah, Z. Catalytic performance of Ag/Fe_2O_3 for the low temperature oxidation of carbon monoxide. *Chem. Eng. J.* **2013**, *219*, 124–130. [CrossRef]
51. Narasimharao, K.; Al-Shehri, A.; Al-Thabaiti, S. Al-Thabaiti, Porous Ag-Fe_2O_3 nanocomposite catalysts for the oxidation of carbon monoxide. *Appl. Catal. A* **2015**, *505*, 431–440. [CrossRef]
52. Bao, S.X.; Yan, N.; Shi, X.H.; Li, R.; Chen, Q.W. High and stable catalytic activity of porous Ag/Co_3O_4 nanocomposites derived from MOFs for CO oxidation. *Appl. Catal. A* **2014**, *487*, 189–194. [CrossRef]
53. Pan, L.; Tang, J.; Chen, Y.H. Synthesis of Fe_3O_4, Fe_2O_3, Ag/Fe_3O_4 and Ag/Fe_2O_3 nanoparticles and their electrocatalytic properties. *Sci. China Chem.* **2012**, *56*, 362–369. [CrossRef]
54. Bai, B.Y.; Qiao, Q.; Arandiyan, H.; Li, J.H.; Hao, J.M. Three-Dimensional Ordered Mesoporous MnO_2-Supported Ag Nanoparticles for Catalytic Removal of Formaldehyde. *Environ. Sci. Technol.* **2016**, *50*, 2635–2640. [CrossRef] [PubMed]

55. Ivanova, A.S.; Slavinskaya, E.M.; Stonkus, O.A.; Gulyaev, R.V.; Glazneva, T.S.; Noskova, A.S.; Boronin, A.I. Highly active and durable Pd/Fe_2O_3 catalysts for wet CO oxidation under ambient conditions. *Catal. Sci. Technol.* **2016**, *6*, 3918–3928. [CrossRef]
56. Ayastuy, J.L.; Iriarte-Velasco, U.; Gurbani, A.; Gutierrez-Ortiz, M.A. Investigation of the calcination temperature effect on the interaction between Au nanoparticles and the catalytic support Au/Fe_2O_3 for the low temperature CO oxidation. *J. Taiwan Inst. Chem. Eng.* **2017**, *75*, 18–28. [CrossRef]
57. Wang, F.; Dai, H.; Deng, J.; Bai, G.; Ji, K.; Liu, Y. Manganese oxides with rod-, wire-, tube-, and flower-like morphologies: Highly effective catalysts for the removal of toluene. *Environ. Sci. Technol.* **2012**, *46*, 4034–4041. [CrossRef] [PubMed]
58. Guldur, C.; Balikci, F. Selective carbon monoxide oxidation over Ag-based composite oxides. *Int. J. Hydrog. Energy* **2002**, *27*, 219–224. [CrossRef]
59. Horcajada, P.; Surble, S.; Serre, C.; Hong, D.Y.; Seo, Y.K.; Chang, J.S.; Greneche, J.M.; Margiolaki, I.; Ferey, G. Synthesis and catalytic properties of MIL-100(Fe), an iron(III) carboxylate with large pores. *Chem. Commun.* **2007**, *27*, 2820–2822. [CrossRef] [PubMed]

© 2017 by the authors. Licensee MDPI, Basel, Switzerland. This article is an open access article distributed under the terms and conditions of the Creative Commons Attribution (CC BY) license (http://creativecommons.org/licenses/by/4.0/).